Scalable cooling cementitious Composites: Synergy between Reflective, Radiative, and Evaporative cooling

Daoru Liu [a,b], Anna Kaja [b], J.C.O. Zepper [b], Daiwei Fan [c], Dongyu Zhang [d], H.J.H. Brouwers [b], Qingliang Yu [a,b,*]

[a] *School of Civil Engineering, Wuhan University, Wuhan 430072, PR China*
[b] *Department of the Built Environment, Eindhoven University of Technology, 5600MB, Eindhoven, the Netherlands*
[c] *Department of Electrical Engineering, Eindhoven University of Technology, 5600MB, Eindhoven, the Netherlands*
[d] *Department of Chemical Engineering and Chemistry, Eindhoven University of Technology, 5600MB, Eindhoven, the Netherlands*

ARTICLE INFO

ABSTRACT

Promoting the sustainability of the building industry is one of the major approaches to addressing energy depletion and climate change. Here, we developed scalable cementitious cooling composites (CCCs) with superior energy-free cooling performance and environmental applicability. Optical properties, phase composition, microstructure, and silica reactivity of composites are characterized and analyzed. Onsite measurements are conducted to evaluate the surface/internal cooling capacities and validate the cooling principles and such composites' climatic applicability. Results show that calcite, C—S—H phases (especially tobermorite), and a higher water-to-powder ratio can increase the solar reflectivity (R_{sun}). Meanwhile, C—S—H and calcite can also increase the spectral emissivity in the atmospheric window (ε_{aw}). Optimal sizes of 0.5 μm (particles) and 1.0 μm (pore size) for Mie scattering are determined by Finite-Difference Time-Domain simulations. The R_{sun} of 0.90 and ε_{aw} of 0.88 are simultaneously achieved, which are comparable to exquisitely designed polymer-based coatings, metamaterials, and multi-layer composites. The surface cooling of 17.3 ℃, internal cooling of 9.2 ℃ by solar reflection, internal cooling of 4.8 ℃ by evaporative cooling, and internal cooling above 2.8 ℃ by mid-infrared (MIR) emission are observed. CCCs are proven to provide efficient cooling in different conditions, with low investment, facile production, and high environmental resistance.

1. Introduction

"Extreme summer" is occurring worldwide, causing significant consequences to human society, due to climate change [1–5]. Cooling facilities are extensively applied in buildings to improve local thermal comfort. However, they consume considerable amounts of energy, resulting in an overall heating effect, especially in tropical and subtropical regions [6,7]. Therefore, efficient and energy-free technologies with desirable cooling performance are in great demand to counter climate change, especially from the perspective of sustainability. Besides thermodynamically improving the energy efficiency of cooling facilities, passive approaches for building thermoregulation including thermochromic hydrogel, highly-oriented thermal conductive films, phase change materials, and passive radiative cooling were studied [8–11]. Radiative cooling is considered one of the most promising pathways thanks to its high efficiency and wide application range.

Traditional radiative cooling requires materials with both high solar spectral reflectivity (λ = 0.28 μm $\sim$ 2.5 μm, R_{sun}) and high mid-infrared (MIR) spectral emissivity in the atmospheric window (λ = 8 μm $\sim$ 13 μm, ε_{aw}). Functional white pigments including oxides (Al_2O_3, SiO_2, etc.), salts ($BaSO_4$, $CaCO_3$, etc.), and polymers (PETE, PVDF-HFP, etc.) with strong superior solar reflection/scattering capacity and infrared absorption bonds (Si-O, Al-O, –CH_2, C—O, C-F, etc.) are generally used [12–15]. They are designed mainly in three forms: 1) particles embedded with the polymer latexes, 2) metamaterials with photonics surface, and 3) multi-layer of oxides/polymers/metals to optimize the chromatic, photonic, and infrared properties [11,14,16–18]. However, the low environmental resistance and durability of these composites are concerns, and the complex fabrication process and high cost also limit their scalable application [14,19].

Cement-based materials, as the most commonly used and cost-effective materials for building envelopes, are generally considered

---

* Corresponding author.
  E-mail address: q.yu@bwk.tue.nl (Q. Yu).

"solar absorbers" however intrinsically durable, porous, C—O/Si-O/ Al-O rich, and hydrophilic. Moreover, cement-bound products are known for their long-term weathering resistance. This study is expected to transfer cementitious materials from building "heater" to "cooler", by utilizing the controllable chromatic/photonic, superior infrared emission, and porous properties [16]. The R_{sun} of cementitious cooling composites (CCCs) can be improved by optimizing the chromatic and photonic properties/Mie scattering. Firstly, fillers and hydration/carbonation products with high whiteness and bandgap can ensure low colorimetric and photonic solar absorption [20]. Secondly, the Mie scattering is excited when the size of the refractive index interface approaches the wavelength of incident light [17,21]. For cementitious composites, refractive index interfaces (air–solid interfaces, ASIFs) mainly exist in two forms: 1) solid (matrix)–air (pores)–solid (matrix) and 2) air–solid (particles/surface structures/hydrates)–air. The former is affected by pore size distribution, while the latter is controlled by the particle size distribution of additives, surface topology, and morphology of hydration products [22]. For example, the crystal morphology of tobermorite can be controlled by autoclaving to provide nano/micro-ASIFs [23,24]. However, the mechanism of ASIFs affecting the R_{sun} and ε_{aw} of cementitious composites, e.g. the exact size and magnitude of ASIFs, has been never investigated. Curing conditions, like moist curing and autoclave, and environmental, like carbonation, during the engineering service, could significantly influence ASIFs. Moisture curing can increase the R_{sun} but the mechanism was not yet clear [25]. The impact of carbonation on the optical properties of CCCs is still unclear due to the complex physicochemical process involved. The different basic optical properties and carbonation mechanisms of hydrates and the corresponding microstructure evolution could result in different variations in R_{sun} and ε_{aw} upon carbonation [26,27]. Hence, a comprehensive understanding of carbonation on R_{sun} and ε_{aw} of CCCs needs to be clarified. Silica is a common additive for both cementitious and radiative-cooling systems. The control of its reactivity is expected to enhance the radiative cooling of cementitious composites. Physically, unreacted nano/micro-silica particles could scatter solar radiation. Chemically, silica could react with alkali and generate calcium silicate hydrates (xCaO·ySiO$_2$·zH$_2$O, C—S—H), then affecting R_{sun} and ε_{aw} [28]. However, this still lacks systematic understanding.

Meanwhile, the evaporative cooling of cementitious composites has not been publicly reported as far as we know while other porous media like metal–organic frameworks (MOFs) have been intensively studied for building cooling [29]. Evaporative cooling of porous media is achieved by utilizing the free water inside the matrix that possesses superior sensible heat capacity and phase transition latent heat. However, the cooling potential of the moisture inside the cementitious matrixes has not been revealed. The evaporative cooling performance is more controlled by capillary porosity and hydrophilicity [29,30]. Since cementitious materials are intrinsically hydrophilic, capillary porosity should be the principal parameter affecting the evaporative cooling and a higher porosity would be beneficial. However, it is noted that the strong solar absorption of H$_2$O molecules would induce a lower R_{sun}. So, the overall cooling capacity of the moisture inside the cementitious matrixes needs to be revealed. Besides the properties of CCCs, the weather conditions, e.g. the cloudage could strongly affect the cooling performance due to its influence on the downward solar irradiation and upward MIR emission. The coupling effect of these two thermal processes on the cooling capacities of CCCs needs to be understood.

In this study, cementitious cooling composites are prepared with different methods, and the phase composition and microstructure are altered by adjusting mixes and curing conditions to investigate their impacts on the optical properties, radia-tive cooling, and evaporative cooling performance of CCCs [31,32]. Physicochemical properties of CCCs are characterized by multi-technics, scattering behaviors of particles and pores are investigated by finite-difference time-domain (FDTD) simulations, and the cooling capacities of CCCs are obtained by on-site measurements. Results reveal the significance of the content/mineralogy of C—S—H and the magnitude of pores on R_{sun}, the chemically-immobilized [SiO$_4$]$^{4-}$ in C—S—H on ε_{aw}, and the evaporative cooling on the overall cooling. Specifically, R_{sun} of 0.90 and ε_{aw} of 0.88 are simultaneously achieved under autoclave curing, which are comparable to exquisitely designed polymer-based and multi-layer composites and metamaterials. Different scattering behaviors of particles and pores are determined and the optimal sizes are recommended. Furthermore, the superior cooling performance under different conditions also shows the excellent environmental applicability and scalability of cementitious cooling composites.

2. Experimental section

2.1. Materials & samples fabrication

White Portland cement (CEM I 52.5 R, Aalborg White), calcium carbonate (≥99 %, Sigma Aldrich), α-quartz powder (SF 300, Quarzwerke), and rutile TiO$_2$ (902P, Chemours) are utilized for composite preparation. The chemical composition of the white cement can be found in Table 1. Powders of each recipe are firstly mixed (3 min) in a disc mill (RS 300, Glenmill) for homogeneity before sample preparation. Particle size distributions of milled recipes are presented in Fig. 1. Superplasticizer (ViscoFlow-3000, Sika) is used to adjust the consistency of the mixtures. Fresh mixtures of each recipe are cast into molds ($4 \times 4 \times 16$ cm^3) and encapsulated by plastic sheets to prevent moisture loss and CO$_2$ exposure. After 1 d encapsulation, samples are demolded and cut into slices ($4 \times 4 \times 1$ cm^3), then for curings as presented in Table 2. Curing conditions and parameters are presented in Table 3. It is noted that only one curing condition is applied to each mix for the sake of simplicity. We would like to stress here that the aim of varying the mix design and curing conditions was not to investigate the effects of initial composition and curing condition on the phase composition and microstructure but to use these variables as a tool to control the phase composition and microstructure. In total 6 different mixes are prepared and labeled as R, Q, L, H1, H2, and H3. The curing method is specified with "M" for moisture (28 d), "C" for carbonation (28 d), and "A" for autoclave (0.25 d), respectively (Table 1). As a consequence, we are able to determine the major effects of phase composition and microstructure on the thermoregulatory.

Table 1
Chemical composition of the white cement.

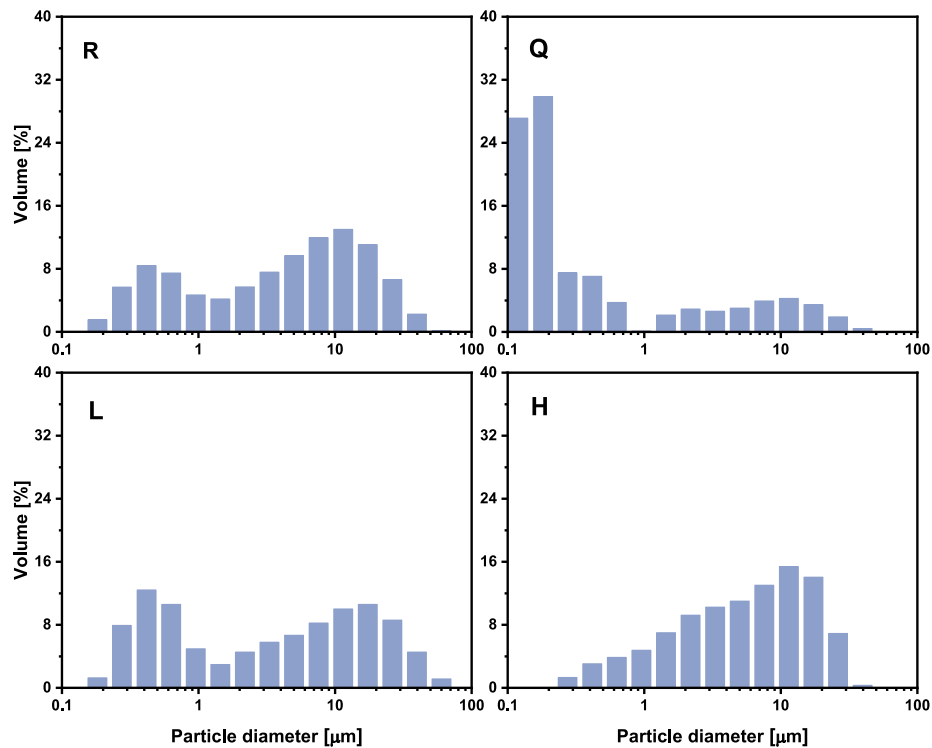| Oxides	Content [wt. %]
CaO	72.89
SiO$_2$	19.59
Al$_2$O$_3$	1.63
SO$_3$	1.65
Fe$_2$O$_3$	0.37
K$_2$O	0.05
SrO	0.15
TiO$_2$	0.07
MnO	0.03
V$_2$O$_5$	0.02
Cl	0.20
LOI (1000 ℃)	3.24

Fig. 1. The particle size distribution of mixed powders of each mix design.

Table 2
Mix design and procedure of cementitious cooling composites.

Curing[1]			Sample	Powder [wt. %]				w/p[2]	SP/w[3]
M	C	A		cement	quartz	CaCO$_3$	TiO$_2$		
√	√	/	R	83.3	/	/	16.7	0.25	0.40
√	√	/	Q	33.3	50.0	/	16.7	0.25	0.40
√	√	/	L	33.3	/	50.0	16.7	0.25	0.40
√	/	√	H1	33.3	25.0	25.0	16.7	0.25	0.40
√	/	√	H2	33.3	25.0	25.0	16.7	0.35	0.29
√	/	√	H3	33.3	25.0	25.0	16.7	0.45	0.22

Mix procedure

Powders — 75% water — 25% water + SP — End
Low speed — Low speed — High speed
Mix time [min]: 0 1 2 3 4 5

[1] In the main text, H2-A-D means the autoclaved (A) H2 sample dried at 70℃ for 24 h (D), and L-C means the sample L with carbonation curing (C).
[2] w/p = mass$_{water}$/mass$_{powder}$.
[3] SP/w = mass$_{superplasticsizer}$/mass$_{water}$.

Table 3
Parameters of three curings.

Curing	Temperature [℃]	Pressure [Bar]	Relative humidity [%]	Duration [d]	CO$_2$ [%]
M−Moist[1]	20	1	/	28	0
C-Carbonation	20	1	65	28	3
A-Autoclave	∼185	∼11	100[2]	∼0.25[3]	0

[1] Cut plates are immersed in tap water.
[2] The autoclave chamber is filled with steam during operation.
[3] The total duration of the autoclave process is about 7 h, including 30 min linear heating and 30 min linear cooling.

2.2. Experimental characterization

2.2.1. Optical properties

Cooling slices ($4 \times 4 \times 1.5$ cm^3) are polished with SiC papers at P400 and then the polished surfaces are cleaned by a high-pressure blower to remove the residual. Hemispherical reflection spectra ($\lambda \sim 0.28$ μm -2.5 μm) of CCCs are obtained using a UV–vis-NIR spectrometer (Lambda 750, PerkinElmer) equipped with a 150 mm integrating sphere, with a scanning interval of 2 nm. The solar spectral reflectivity (R_{sun}) is calculated by:

$$R_{sun} = \frac{\int_{0.28\mu m}^{2.5\mu m} I_{sun}(\lambda)R(\lambda)d\lambda}{\int_{0.28\mu m}^{2.5\mu m} I_{sun}(\lambda)d\lambda} \tag{1}$$

Where,

λ is the wavelength [μm],

$R(\lambda)$ is the reflectance spectrum of cooling slices,

$I_{sun}(\lambda)$ is the global solar intensity spectrum at sea level from [33].

Fourier transform infrared (FTIR) spectrometer (Nicolet iS50, Thermo Fisher) equipped with a gold-coated integrating sphere (Mid-IR IntegratIR^{TM}, PIKE technologies) is used to measure the absorptance spectra of CCCs at 400 cm^{-1}-4000 cm^{-1} range, with a scanning interval of 0.5 cm^{-1}. Based on Kirchhoff's thermal irradiation law, the thermal emissivity equals absorptance for the untransparent object [13]. Hence, the spectral emissivity in the atmospheric window (ε_{aw}) is calculated by:

$$\varepsilon_{aw} = \frac{\int_{8\mu m}^{13\mu m} \sigma(\lambda)I_B(\lambda)d\lambda}{\int_{8\mu m}^{13\mu m} I_B(\lambda)d\lambda} \tag{2}$$

$$I_B(\lambda, T) = \frac{C_1}{\lambda^5(e^{C_2/\lambda T} - 1)} \tag{3}$$

Where,

$\sigma(\lambda)$ is the absorption spectrum of cooling slices,

$I_B(\lambda)$ is the spectral emission power of the blackbody [W/m^3],

C_1 is 3.743×10^{-16} W·m^2,

C_2 is 1.4387×10^{-2} m·K.

It is noted that the surface temperature can affect $\sigma(\lambda)$ and $I_B(\lambda)$, and the temperature defaults to 300 K in this study.

UV–vis spectrometer (USB 4000, Ocean Optics) equipped with a halogen light source (HL-2000-FHSA, Ocean Optics) is used to obtain the *CIE* whiteness of cooling composites. For each sample, 50 scans are performed in a sweeping method.

2D FDTD simulations are conducted in Matlab to investigate the scattering behaviors of particles and pores, by solving Maxwell's equations. Two representative wavelengths of incident radiation (1.0 and 2.0 μm) and three sizes (0.5, 1.0, and 2.0 μm) of particles and pores are adopted. Particles are assumed to be the semi-circle (solid) above the cementitious matrix surface, while pores are assumed to be the semi-circle (void) below the cementitious matrix surface. The source codes can be found in Supplementary Materials.

2.2.2. Phase composition

CCCs are ground with an XRD mill (Mill McCrone, Retsch) to powder which is then scanned by an XRD analyzer (D4, Bruker) with a Co tube (40 kV, 40 mA), scanning interval of 0.02°/min, residence time of 0.5 s, and 2θ from 10° to 90°. The quantitative XRD analysis is conducted by TOPAS (Bruker) using 10 wt% pure silicon as the standard.

FTIR spectrometer (Frontier, PerkinElmer) at 400–4000 cm^{-1} range and resolution of 1 cm^{-1} are used to analyze the mid-infrared absorption of raw materials and granulated hardened pastes with the attenuated total reflection (ATR) crystal (GladiATR,

PIKE Technologies). It is noted that the Frontier FTIR is used to obtain the relative MIR absorption intensity of materials, using air as the background.

2.2.3. Microstructure

A mercury porosimeter (AutoPore V9500, Micromeritics), working with the absolute pressure from 0.7 kPa to 227.5 MPa and the contact angle of 130°, is used to obtain the porosity and pore size distribution of composites. The pore number at a certain pore radius is calculated by:

$$S = \frac{V}{4/3\pi r^3} \tag{4}$$

Where,

S is the pore number [g^{-1}],

Is the incremental pore volume [m^3/g],

r is the pore radius [m].

Scanning electron microscopy (JSM-IT100, Jeol) is used to observe the microstructure of composites and the morphology of tobermorite. Crushed thin pieces are placed on holders with the conductive tape and Pt-coated for 60 s (65 mA) with the sputter coater (K550X, Emitech).

2.3. Cooling performance measurement

Cooling specimens with the dimensions of $4 \times 4 \times 1$ cm^3 are used for the on-site measurement on the experimental platform as shown in Fig. 2 (SolarBEAT Roof, Vertigo Building, Eindhoven University of Technology). The platform consists of three insulation boxes ($10 \times 10 \times 10$ cm^3), a pyranometer (MS802, EKO Instruments), a sun tracker (STR220, EKO Instruments), a wind sensor (V200A Ultrasonic, Lufft), three thermistor sensors (NTC, SENSOR DATA, $\pm$ 0.05 °C), and a data logger (SQ2040, Grant). The insulation box is made of three insulation layers, a steel base, and aluminum foil. The thickness of each insulation layer is 2 cm, while the thermal conductivities of the extruded polystyrene (XPS, JACKODUR Plus 300 Standard, Jackson insulation) layer and SiO$_2$ aerogel (IC3100, Cabot) layers are 0.027 W/(m·K) and 0.012 W/(m·K), respectively. The steel base is to keep the stability of the box, while the insulation layers and reflective foil are used to minimize the thermal gain of the box. An infrared camera (B360, FLIR) is used to get thermal images with the default emissivity of 0.9. It is noted that this emissivity is set to measure the surface temperature of cementitious materials (cooling composite, commercial cement paste, and cement mortar floor) and could not provide the actual surface temperature of the aluminum foil. It is noted that all the measured temperatures (both surface and internal) of the slice installed on the insulation box are to demonstrate the cooling performance of as-prepared materials. Field study is further needed to clarify their performance in real engineering practice.

2.4. Cooling capacity estimation

Multiple heat exchange processes are involved in the energy balance of the insulation box, and the cooling capacity can be estimated by,

$$P_{net} = P_{rad} + P_{hyd} - P_{sun} - P_{atm} - P_{con} - P_{lea} \tag{5}$$

Where,

P_{net} is the net cooling power [W/m^2],

P_{rad} is the cooling power by MIR emission [W/m^2],

P_{hyd} is the evaporative cooling power [W/m^2], P_{sun} is the heating power of solar radiation [W/m^2],

P_{atm} is the heating power of downward atmosphere radiation [W/m^2],
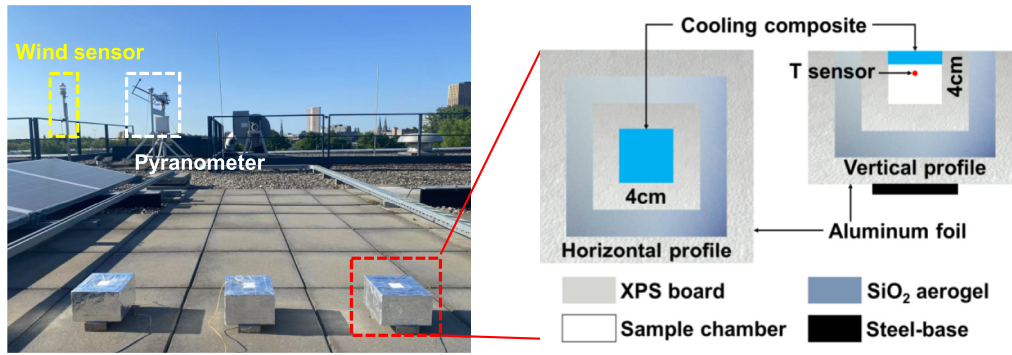
Fig. 2. Schematic of the on-site experimental platform.

P_{con} is the heating power of heat conduction through the box envelope [W/m^2],

P_{lea} is the heating power of thermal leakage through the contact surface (wherever not 100 % air-tight) of the box envelope [W/m^2].

P_{rad} increases with the increase of ε_{aw}, P_{hyd} increases with the increase of porosity, P_{sun} decreases with the increase of R_{sun}, P_{atm} is above 0 and increases with the increase of cloudage [34], P_{con} is mainly determined by the internal/outdoor temperature difference and thermal conductivity of the cooling composite (Section 2.3), P_{lea} is approximately zero owing to the good air tightness.

3. Results & discussions

Mixes R, Q, and L with different initial compositions are moisture and carbonation cured, mixes H1, H2, and H3 were moisture and autoclaved cured and have different w/p ratios. In total 12 samples are investigated with a multi-analytical approach to figure out the impacts of phase composition and microstructure on the three thermoregulatory principles.

3.1. Whiteness of cooling composites

Fig. 3a shows the whiteness of cooling composites cured under different conditions. The color of a homogeneous matrix is determined by the basic chromas and proportions of components. The addition of quartz decreases the whiteness of CCCs while the addition of calcite shows a reversed impact. Autoclaved samples show the highest whiteness, while carbonation induces a drop in whiteness. Autoclave curing can promote the pozzolanic reaction between quartz and portlandite for more C—S—H and also increase the crystallinity of C—S—H [24]. The C—S—H amounts (amorphous C—S—H + crystallized C—S—H + tobermorite) in H1-A, H2-A, and H3-A are all about 55 wt%, but only the increase of the tobermorite content obviously increase whiteness (Fig. 5c). This reveals the significance of tobermorite on the whiteness of CCCs and also the different "whitening" capacities of different C—S—H polymorphs. The whiteness of carbonated composites is lower than moisture ones, which could be attributed to the decalcification/decomposition of C—S—H to CaCO$_3$ (mainly amorphous) and silica gel. These reveal the higher "whitening effect" of C—S—H than the portlandite by hydration, and CaCO$_3$ and silica gel by carbonation, which is supported by quantitative phase analysis (Fig. 3b & Fig. 4a) [35]. Meanwhile, a higher w/p is found to increase the whiteness of cooling composites, and it is more prominent for autoclaved composites. Under moisture condition, a higher w/p can promote cement hydration (28d) which leads to more accumulation of C—S—H, which is validated by the strongest peak (2θ = 20.96°) of portlandite in H3-M (Fig. 3c) [24].

3.2. Impact of phase composition on R_{sun} and ε_{aw}

It is noted that phase composition could affect R_{sun} and ε_{aw} of CCCs [36]. However, the basic chromatics (whiteness) and microstructure (e.g. pore structure) are strongly related with phase composition. This section focuses on the impacts of phase composition on these factors and the interactions between phase composition and other parameters like pore structure and whiteness are further discussed.

The substitution of white cement with calcite increases R_{sun} while the use of quartz results in a decrease in R_{sun} (Fig. 4b). The bandgaps of α-quartz (9.5 eV, $\lambda \sim 130$ nm) and calcite (6.0 eV, $\lambda \sim 207$ nm) are both above 4.4 eV ($\lambda \sim 280$ nm), which means that these two non-reactive materials do not affect the solar reflection, regarding the photonic absorption [37,38]. The pore number of
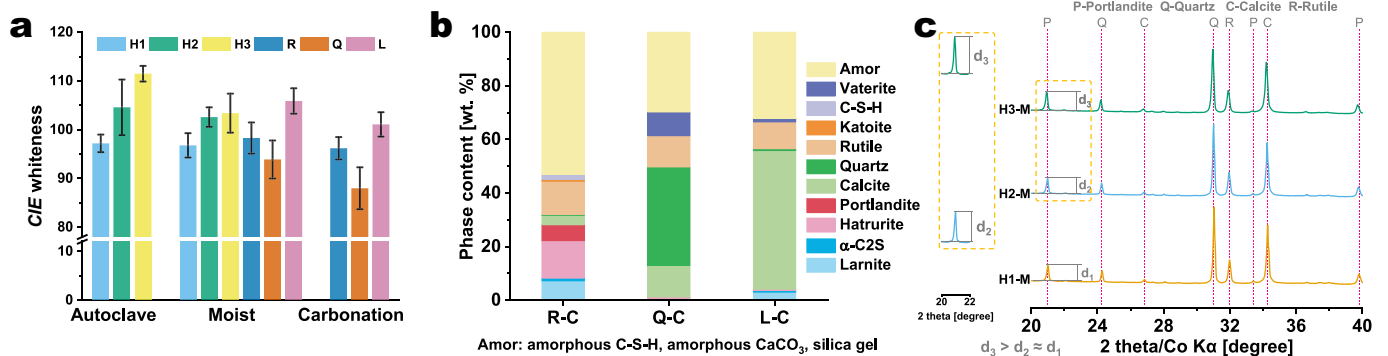

Fig. 3. (a) Whiteness of cooling composites with different phase composition and curing conditions, (b) Phase composition of carbonation-cured composites, and (c) XRD spectra of moisture-cured cooling composites.
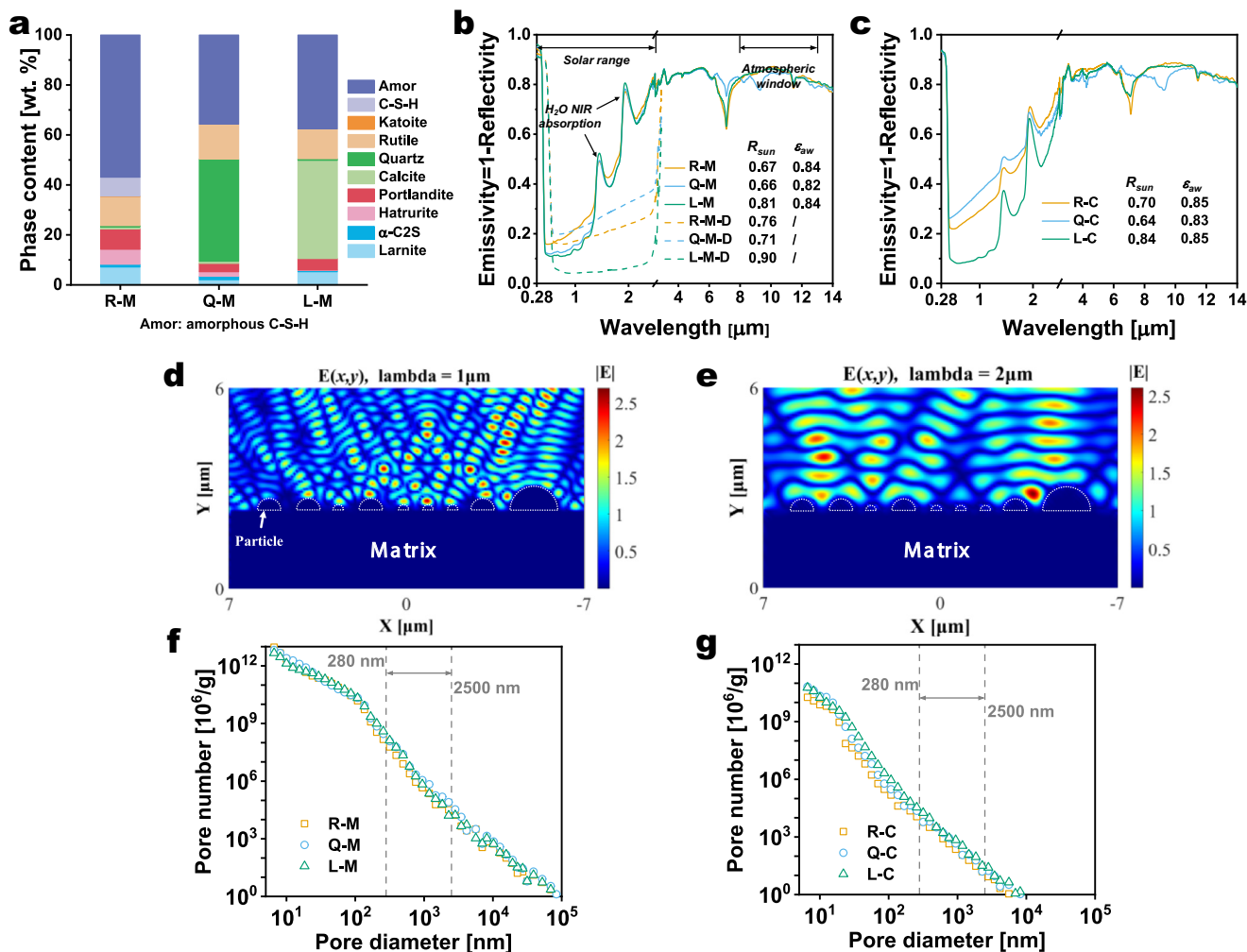
Fig. 4. (a) Phase composition of moisture-cured composites, (b) Emissivity spectra of moisture-cured composites, (c) Emissivity spectra of carbonation-cured composites, (d) Electromagnetic field of particles' scattering at $\lambda = 1$ µm, (e) Electromagnetic field of particles' scattering at $\lambda = 2$ µm, (f) Pore number distribution of moisture-cured composites, and (g) Pore number distribution of carbonation-cured composites.

moisture-cured and carbonation-cured composites in the 280–2500 nm range varies to a similar extent (Fig. 4f&g). Hence, the R_{sun} variation of moisture-cured composites is attributed to the whiteness and the Mie scattering of unreactive particles. More nano/microparticles in L-M with a diameter of 280 nm-2500 nm than in Q-M could scatter more solar irradiation and induce a higher R_{sun} (Fig. 1). Scattering behaviors of particles are simulated. The modeling shows that the nano/microparticles can efficiently scatter the solar irradiation at different wavelengths as shown in Fig. 4d&e. Particles with a size of 0.5 µm in diameter induce a stronger Mie resonance when the incident wavelength is 1.0 µm, while particles with a 1.0 µm diameter induce a stronger Mie resonance when the incident wavelength is 2.0 µm. These indicate that particles with a diameter half of the incident wavelength can scatter more solar radiation. This finding can be utilized to optimize the particle size distribution of fillers for solar reflection. The dominant wavelength of solar radiation is around 0.6 µm, so the optimal particle size for Mie scattering should be around 0.3 µm.

Drying is also found to considerably increase the R_{sun} of CCCs (Fig. 3b). The removal of free water can increase R_{sun} by reducing the NIR solar absorption of H_2O molecules. The R_{sun} of 0.90 is comparable to the polymer-based and multilayer composites [15,19,25,36,39–42]. Upon carbonation, the phase composition and optical property of the cooling composites simultaneously

change (Fig. 3b & Fig. 4c). Compared with moisture-cured composites, more $CaCO_3$ (amorphous, vaterite, and calcite) is observed in carbonated composites as expected, and the R_{sun} of R-C and L-C both slightly increase while Q-C shows a drop with more vaterite. The drop in whiteness and R_{sun} of Q-C is attributed to the yellow chromatics of vaterite [43,44]. The ε_{aw} of cooling composites increases with more $CaCO_3$ while the addition of quartz decreases the ε_{aw}, but all cooling composites have the ε_{aw} above 0.82. This ε_{aw} is also comparable to some polymer-based and multilayer composites that can ensure efficient MIR emission [15,36].

3.3. Impact of nano/micropores on R_{sun} and ε_{aw}

In Section 3.2, the alteration of microstructure upon carbonation is mentioned but it is not straightforward to identify its impact on the R_{sun} and ε_{aw} due to the simultaneous effects of other variables. From Section 3.1, the whiteness variation of moisture-cured composites caused by w/p is limited compared to autoclaved ones. The phase composition of these composites is quite similar according to the XRD analysis (Fig. 3c). Hence, the microstructure is considered the dominant variable for H1-M, H2-M, and H3-M affecting the R_{sun} and ε_{aw}. A gain in R_{sun} of 0.09 is obtained by the microstructure control, which means 9 % more solar radiation is reflected and extra cooling power of 74 W/m² (integrated solar
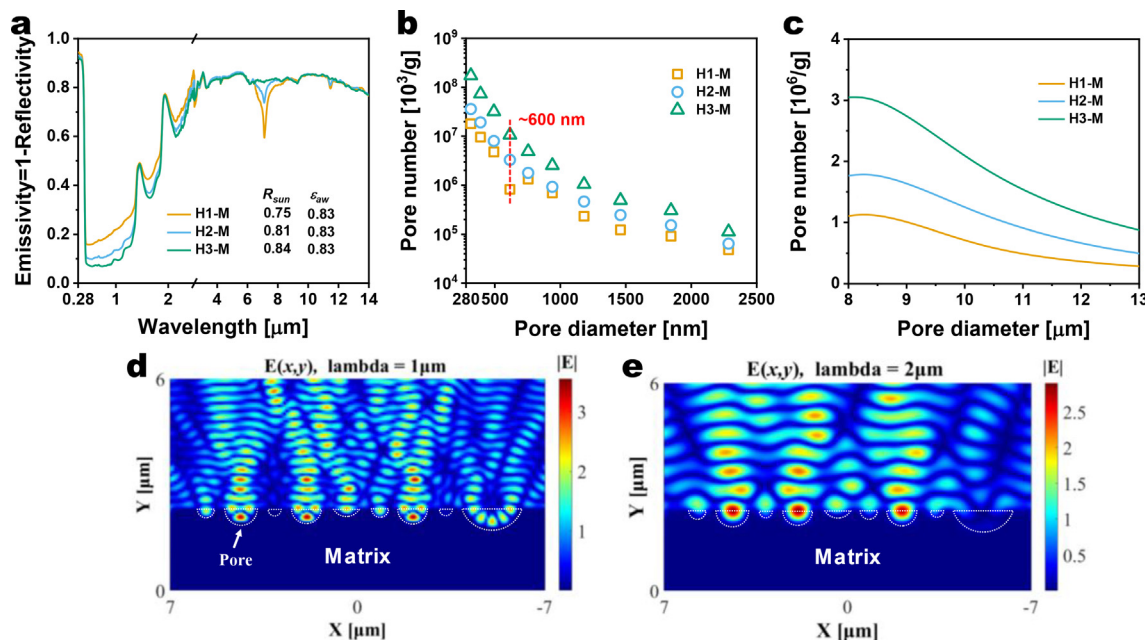
Fig. 5. (a) Emissivity spectra of moisture-cured cooling composites, (b) Pore number distribution in the solar spectral range, (c) Pore number distribution in the atmospheric window range, (d) Electromagnetic field of pores' scattering at λ = 1 μm, and (e) Electromagnetic field pores' scattering at λ = 2 μm.

irradiance: 826 W/m^2), while the ε_{aw} of all composites is the same (Fig. 5a). With the increase of w/p, the pore number in the solar spectral range of composites varies from 10^8/g to 10^{12}/g with the basic magnitude of 10^8/g, and a great difference is observed at the pore diameter of around 600 nm (Fig. 5b). It validates that a higher w/p can create more pores at the solar spectral range and promote the Mie scattering then increase the R_{sun} [21]. The scattering behaviors of pores are different from the particles, as shown in Fig. 5d&e. Pores with a 1.0 μm diameter are found the optimal to trigger Mie resonances when the incident wavelengths are 1.0 μm and 2.0 μm, which can be used for pore structure optimization. The difference in Mie scattering between particles and pores could be attributed to the forms and structures of ASIFs. The pore number in the atmospheric window range of composites varies within the magnitude of 10^6/g, which contributes to the limited impact on ε_{aw}. It also reveals that the impact of pores (Mie scattering) on optical properties is not observable until the pore number reaches a certain magnitude.

3.4. Impact of silica reactivity on R_{sun} and ε_{aw}

In Fig. 6, the R_{sun} of autoclaved composites increases with the increment of w/p, while the ε_{aw} of all autoclaved composites is about 0.88 but higher than other cooling composites in this study and the reported value in another study [36]. It is noted that the dried H3-A also shows the R_{sun} of 0.90 as the dried L-M (Fig. 6c). The pore number in the solar spectral range of autoclaved composites is much fewer than other curing conditions, owing to the "filling effect" of more C—S—H. The pore number magnitude of 1–10^5/g is far below the limit to observe the impact of pores on R_{sun}. Besides, No pores exist in the atmospheric window range according to the calculation in autoclaved samples (Table 4). With the higher w/p, the silica reactivity (quartz residuals) and the crystallinity of C—S—H [(C—S—H + T_11A)/(amor + C—S—H + T_11A)] increase. The Mie scattering by particles of autoclaved composites is almost the same, because of the limited differences in the amount of unreacted fillers (quartz/calcite/rutile/larnite). Referring to Section 3.1, the results demonstrate that the increase in R_{sun} of

autoclaved composites could be attributed to the increased whiteness. More importantly, the nano/micro-sized "acerose and petaloid" crystals of tobermorite also enhance the Mie scattering (Fig. 6e). Our previous study also indicated the morphology of tobermorite could be modified by appropriate measures [23]. The higher MIR emission capacity of chemically-immobilized SiO_2 (SiO_4^{4-}) in C—S—H than silica particles is observed, compared to the moisture-cured composites (Fig. 6f). The reduced Mie scattering of SiO_2 particles in the atmospheric window range could be another reason for this phenomenon. Based on the aforementioned content, the collaboration of silica and autoclave curing can prepare CCCs with desired R_{sun} and ε_{aw}, by optimizing the content, mineralogy, and morphology of C—S—H.

3.5. Cooling performance by thermoregulation

To investigate the impact of solar reflection and evaporative cooling on the overall cooling performance (surface and internal) of the prepared cooling composites, one dried ordinary cement paste slice (Ref-D[1]), one wet cooling slice (L-M), and one dried cooling slice (L-M−D) are installed and tested in a sunny and breezy day, and results are presented in Fig. 7. It is noted that the roof made of cement mortar is used as the background of IR photos.

At the beginning of the monitoring, internal temperatures of Ref-D and L-M−D increase quickly above the ambient temperature within 10 min, while the internal temperature of L-M shows a tiny drop within the first 20 min and then keeps lower than the air temperature for about 2 h (10:00–12:00). The internal temperature of Ref-D is much higher than L-M−D and L-M, and the difference increases with the increment of solar irradiance. Besides, IR photos show the surface cooling of 17.3 ℃ by solar reflection, comparing L-M−D and Ref-D. The internal temperature of L-M is lower than L-M−D for about 5.5 h (10:00–15:30) and higher than L-M−D for the late time (16:00–20:00).

---

[1] This cement paste is made of ordinary Portland cement (CEM I 42.5N, ENCI) with the water-to-binder ratio of 0.4 and then cured for 28d.
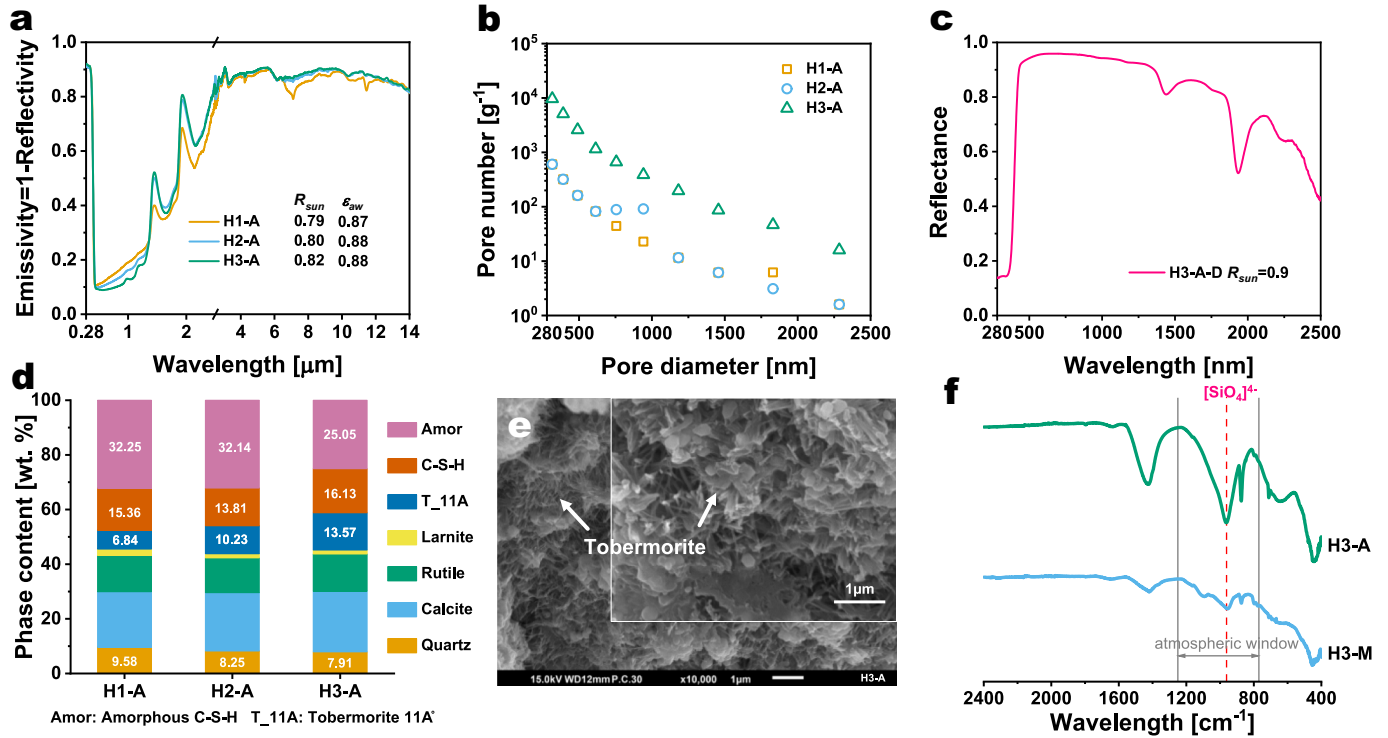
Fig. 6. (a) Emissivity spectra, (b) Pore number distribution in the solar spectral range, (c) Solar reflectance spectrum of dried H3-A, (d) Phase composition of autoclaved cooling composites, (e) SEM graphs of H3-A, and (f) FTIR spectra of H3-A and H3-M.

Table 4
Calculated pore numbers of the autoclaved cooling composites.

Pore diameter [μm]	Pore number [g^{-1}]		
	H1-A	H2-A	H3-A
15.59	0.02	0.02	0.04
12.63	0.02	0.03	0.10
10.19	0.05	0.05	0.22
8.15	0.07	0.11	0.46
6.92	0.12	0.15	0.23

The enhanced solar reflection can provide a surface cooling of 17.3 ℃ and internal cooling of 9.2 ℃ (maximum). The higher the solar irradiance is, the stronger the surface cooling is obtained owing to the larger solar absorption reduction. A temperature difference (internal) of 4.8 ℃ is observed at around 10:40 h between the wet and dried L-M samples, and the internal temperature of the L-M keeps lower than L-M−D till 15:00 h. These results demonstrate that evaporative cooling can provide an extra cooling of 4.8 ℃ (maximum) at the early cooling stage and a net cooling gain throughout the day. Meanwhile, rainfall and manual wetting are expected to reset the evaporative cooling during the long-
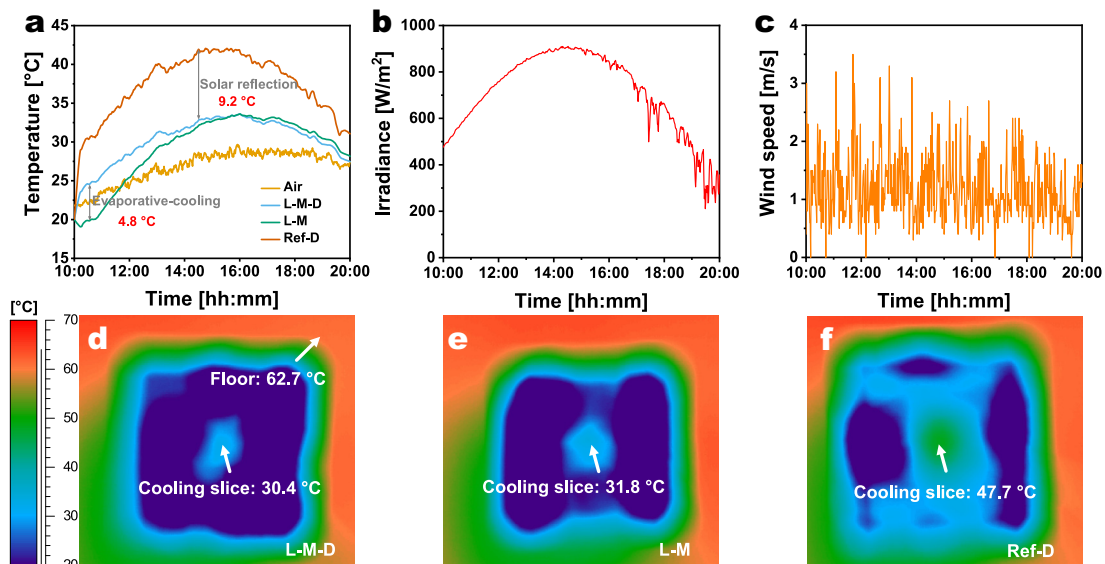

Fig. 7. (a) Temperatures of internals and air, (b) Solar irradiance, (c) Wind speed, and (d-f) IR photos of tested surfaces (4:00 pm).
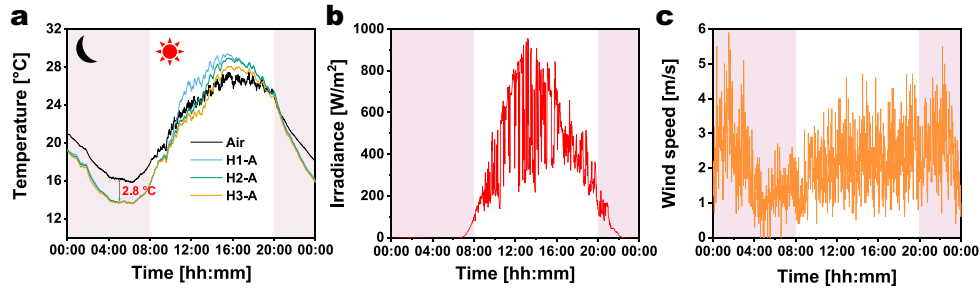
Fig. 8. (a) Temperatures of internals and air, (b) Solar irradiance, and (c) Wind speed.

term service [45]. The smaller day-night temperature variation of the cooling envelope is also expected to reduce the thermal stress and then protect the integrated building structures during hot days [46].

In addition, an internal temperature of about 2.8 ℃ lower than the air is observed in both H1-A, H2-A, and H3-A during the night on a fine day (Fig. 8). The similar nighttime cooling performance is mainly attributed to the similar MIR emission capacity (ε_{aw}) of H1-A, H2-A, and H3-A. P_{hyd} is below 0 (gaseous water changes to aqueous water with heat release), P_{con} is above 0 (air temperature is higher than the internals), and P_{sun} is near 0 in this condition. Hence, this internal cooling is the sum of the P_{rad}, P_{hyd}, P_{con}, and P_{atm}. This means the internal cooling induced by the MIR emission is higher than 2.8 ℃ according to Eq. (5).

3.6. Cooling capacity under different weather conditions

The previous section presents the superior surface and internal cooling capacities of the dried and wet cooling composites, which shows the climatic scalability of CCCs. In the Mid-East and East Africa, the summer is long and extremely dry with almost no precipitation, dried CCCs can provide appreciable cooling effects (Sections 3.3 and 3.5). During the long and hot summers in regions like East Asia, South America, and South Europe, the moisture charge by regular precipitations can provide extra cooling. Besides the regional climate, cloudage as the most important parameter of

microclimate affecting the solar heat gain and MIR emission is investigated in this section.

On a sunny day, the solar irradiance is stable during the whole measurement, so the lower temperature at 14:00–16:00 is attributed to enhanced thermal convection and water evaporation by wind (Fig. 9a-c). The internal temperature varies with the air temperature, while H2-A shows a lower internal temperature than the air for about 1 h, and the internal temperature of H3-A keeps lower than air. This is mainly attributed to evaporative cooling owing to the different volumes of free water inside composites as discussed in Section 3.2 and Section 3.5 (Fig. 9g and Fig. S5). On a cloudy day, internal temperatures vary with the solar irradiance when the wind speed is relatively stable, and they are higher by 2.9–4.2 ℃ than the air temperature (Fig. 8d). The IR photos show the surface cooling of 23.1 ℃ and 16.1 ℃ on sunny and cloudy days, which is in line with the internal temperature measurement.

The surface temperature of the floor on the cloudy day is 7.0 ℃ lower than on the sunny day, but the surface temperatures of the cooling composites are higher on the cloudy day. The solar irradiation from the sun is partially shielded by the cloud, but this limits the solar gain of all cooling composites to a similar extent. This means the surface temperature is more affected by the MIR emission of these cooling composites, which could be attributed to the "MIR shielding impact" of the cloud (H_2O) in the atmospheric window (Fig. 10). These results are in line with previous observation: 1) the wind speed can affect both the air-surface thermal convec-
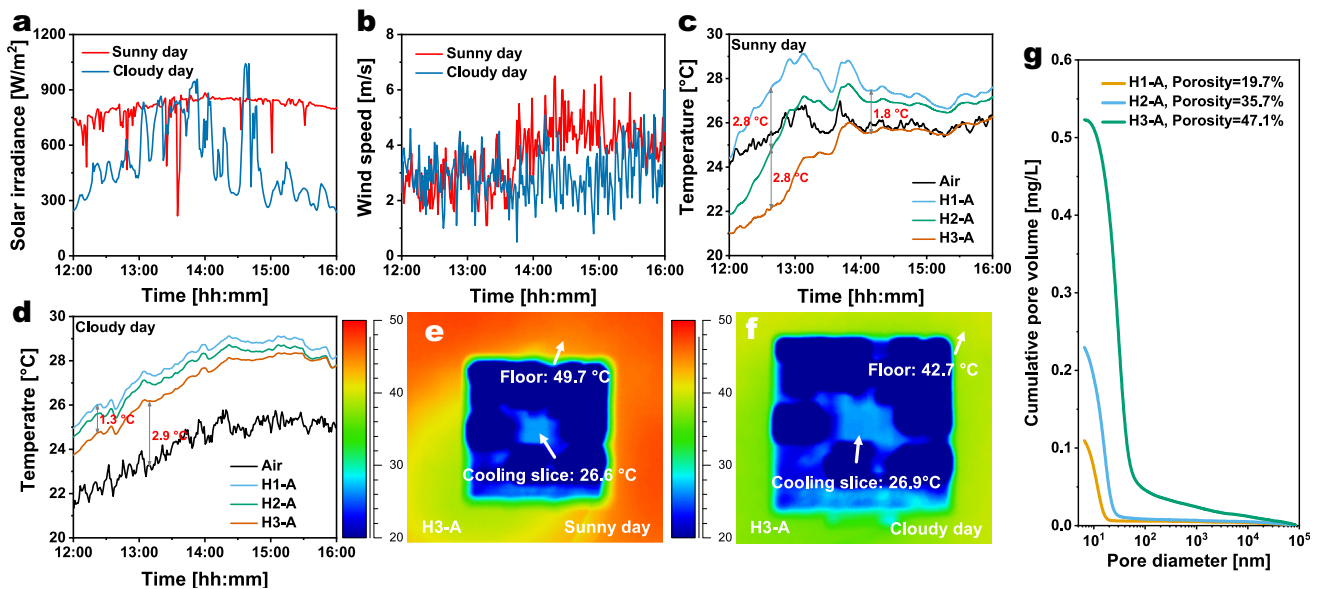

Fig. 9. (a) Solar irradiance, (b) Wind speed, (c & d) Temperature variation, and (e & f) IR photos of H3-A (2:00 pm) and (g) the accumulative pore volumes of autoclaved cooling composites.
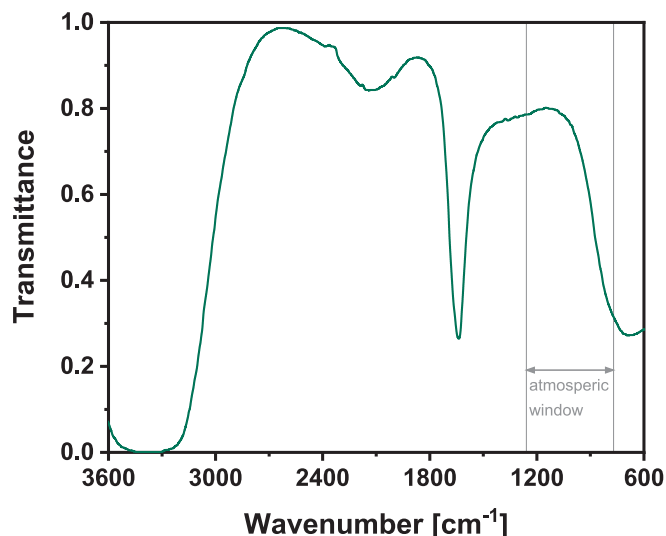
Fig. 10. Infrared transmittance spectrum of H_2O (drawn by data from the Water (nist.gov)).

oped chemical industry and fine expensive machines [15]. Moreover, high environmental resistance owing to the CCCs' strong chemical and physical stability, and climatic applicability owing to the high porosity and hydrophilicity are simultaneously realized. Meanwhile, CCCs can be applied not only in thin panel form but also in various flexible forms of coating/render, block, etc. The advantages ensure the scalable production of CCCs in not only developed countries/areas but also developing areas like Equatorial Africa, Southeast Asia, and South America. The large-scale application of CCCs is expected to efficiently provide passive cooling and contribute to the "Sustainable Development Goals" of the United Nations.

In this work, the high UV absorptance of all CCCs is observed, and a smaller dosage of TiO_2 would address this problem. More natural minerals like limestone and feldspar with superior optical properties after the milling could be utilized to further increase the sustainability and reduce the cost of CCCs. Binder wise, geopolymers could be promising alternatives for radiative cooling because of the controllable phase composition and microstructure [49]. In addition, we are working on finding more effective pathways to modify the surface topology of CCCs to further enhance the Mie scattering.

tion and evaporative cooling and 2) the MIR cooling capacity could be limited due to the "shielding impact" of the cloud [13].

4. Recommendations and considerations

The three thermoregulatory principles are validated and the expected cooling capacities are proven by taking advantage of the physicochemical properties of CCCs (Fig. 11). Compared with traditional cooling building materials, the prepared CCCs show higher R_{sun} which indicates better reflective cooling performance [41,47,48]. Compared with polymer-based and multi-layer coatings/composites, the production of CCCs does not require a devel-

5. Conclusions

In this study, scalable and affordable cementitious cooling composites for energy-free cooling of buildings are developed. Physicochemical properties and cooling performance of CCCs under different conditions are tested to validate the cooling principles and capacities. C—S—H and calcite are found to increase the whiteness, R_{sun}, and ε_{aw} of CCCs, while the role of C—S—H mineralogy is determined, especially the strongest "whitening effect" and possible scattering impact of tobermorite. More chemically-bound silica $[SiO_4]^{4-}$ in C—S—H can provide a higher ε_{aw} by increasing the reactivity of silica in cementitious systems. The Mie scattering can be enhanced by optimizing the size of particles and pores, and the
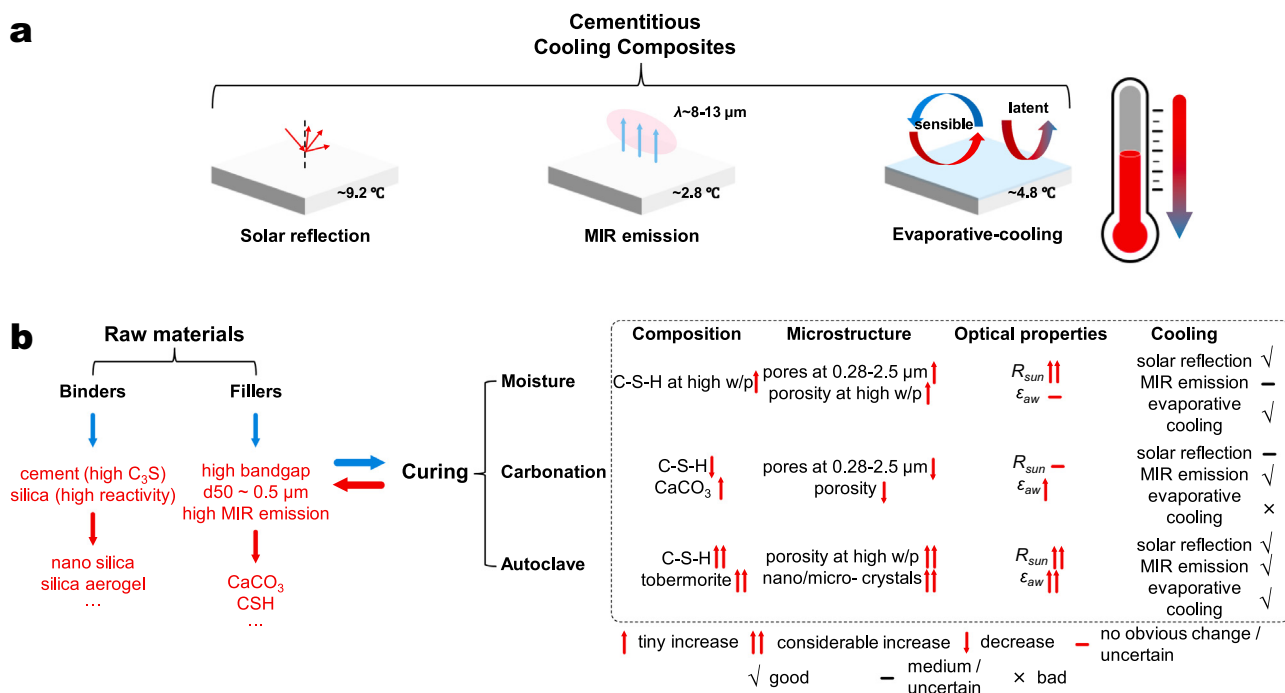

Fig. 11. (a) Cooling principles and capacities of CCCs, and (b) Flow chart of initial materials, curings, physicochemical properties, and cooling performance of CCCs.

morphology of tobermorite. The highest R_{sun} of 0.90 and ε_{aw} of 0.88 are obtained at the autoclave condition, and they are comparable to some exquisitely designed polymer-based coatings, metamaterials, and multi-layer composites. Onsite measurements show the surface cooling of 17.3 ℃ and internal cooling of 9.2 ℃ by solar reflection and internal cooling by MIR emission above 2.8 ℃. The free water inside CCCs can provide an internal cooling of 4.8 ℃ although the NIR absorption of H_2O molecules induces the R_{sun} increment. CCCs are verified that can be applied in various regions with different climate conditions for efficient cooling.

Data availability

Data will be made available on request.

Declaration of Competing Interest

The authors declare that they have no known competing financial interests or personal relationships that could have appeared to influence the work reported in this paper.

Appendix A

The drop on the surface of CCCs is completely absorbed in a short time as shown in Fig. S2a. Fig. S2b was taken at the 91st count.
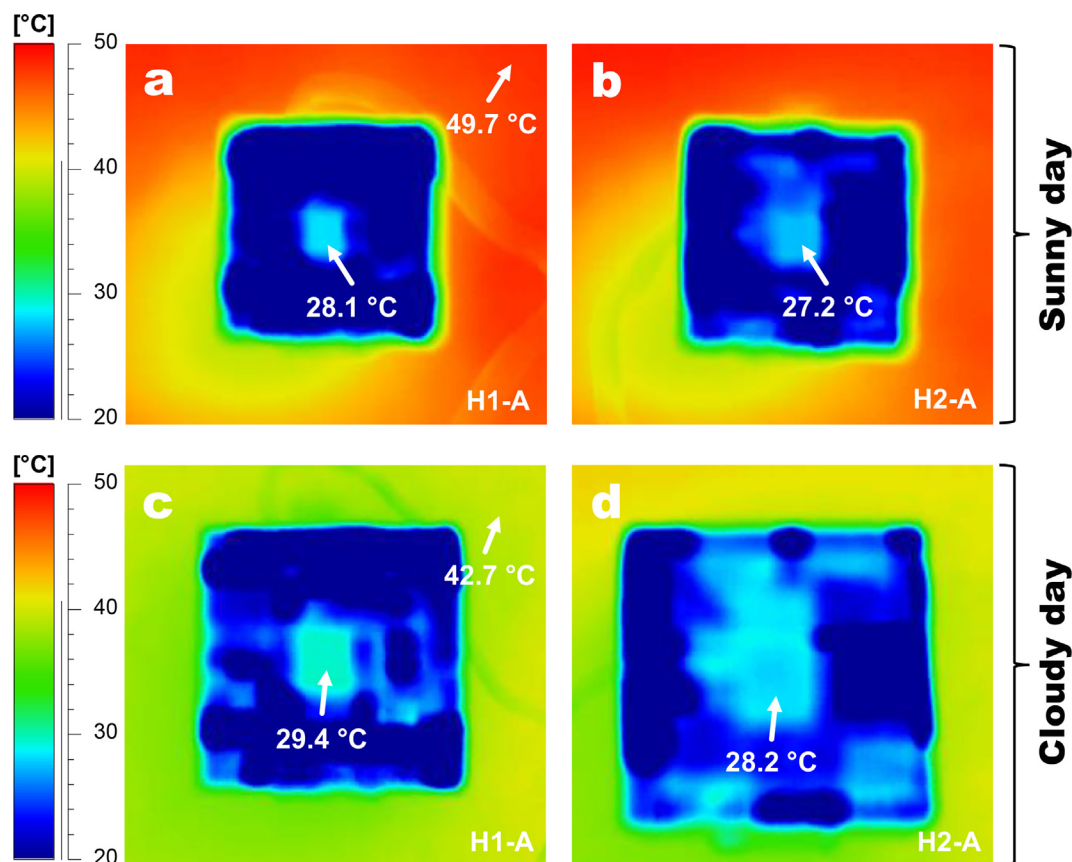

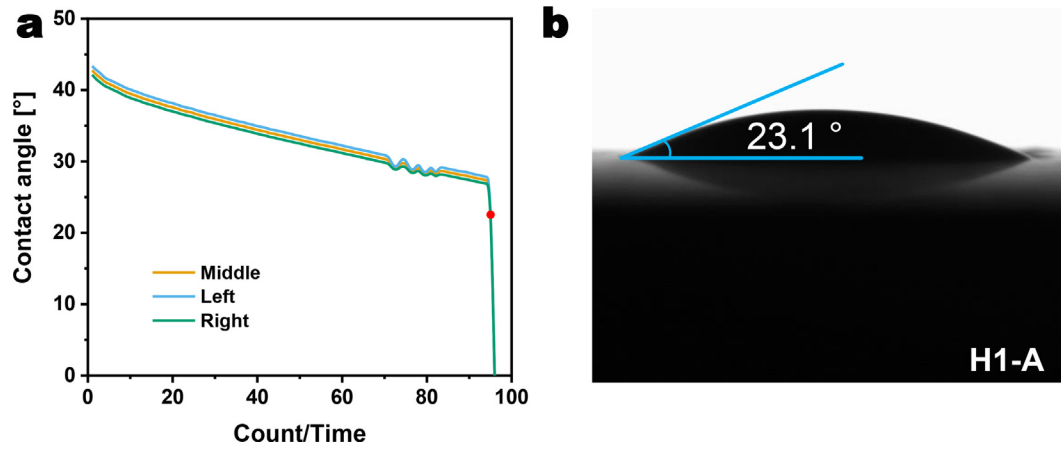**Fig. S1.** (a) IR photos of H1-A and H2-A on (a&b) the sunny day and (c&d) the cloudy day.

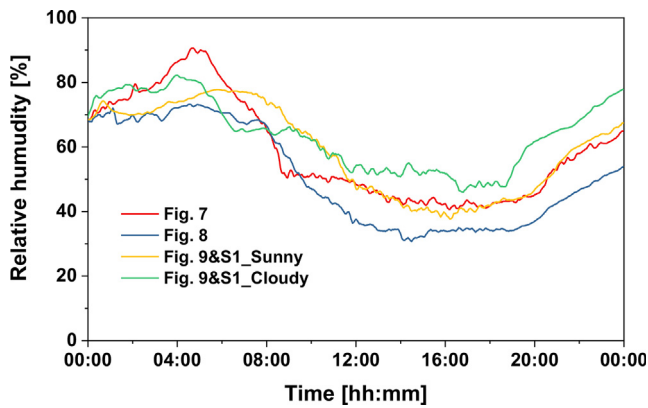**Fig. S2.** (a) Contact angle of H1-A and (b) photo of contact angle (the red point at the left graph).

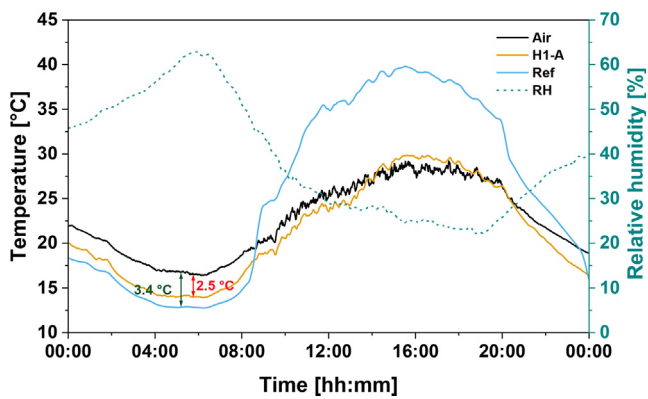**Fig. S3.** Relative humidity variations during the outdoor measurements.

Fig. S5. Mass loss of autoclaved samples by drying (70 °C, 24 h).

Fig. S4. Temperatures of air/internals and relative humidity during the outdoor measurement.

Table S1
Summary of R_{sun} and ε_{aw} of prepared samples.

Sample label	R_{sun}	ε_{aw}
R-M	0.67	0.84
Q-M	0.66	0.82
L-M	0.81	0.84
R-M-D	0.76	/
Q-M-D	0.71	/
L-M-D	0.90	/
R-C	0.70	0.85
Q-C	0.64	0.83
L-C	0.84	0.85
H1-M	0.75	0.83
H2-M	0.81	0.83
H3-M	0.84	0.83
H1-A	0.79	0.87
H2-A	0.80	0.88
H3-A	0.82	0.88
H3-A-D	0.90	/
Ref	0.27	0.96
Ref-D	0.30	/

Appendix B. Supplementary data

Supplementary data to this article can be found online at https://doi.org/10.1016/j.enbuild.2023.112909.

References

[1] L. Li, Y. Zha, Science of the Total Environment Mapping relative humidity, average and extreme temperature in hot summer over China, Sci. Total Environ. 615 (2018) 875–881, https://doi.org/10.1016/j.scitotenv.2017.10.022.

[2] E. Im, N. Thanh, Y. Kim, J. Ahn, 2018 summer extreme temperatures in South Korea and their intensification under 3 °C global warming, Environ. Res. Lett. 14 (2019), https://doi.org/10.1088/1748-9326/ab3b8f.

[3] Z. Zhong, X. Chen, X.-Q. Yang, Y. Ha, Y. Sun, The relationship of frequent tropical cyclone activities over the western North Pacific and hot summer days in central-eastern China, Theor. Appl. Climatol. 138 (3-4) (2019) 1395–1404.

[4] V. Weilnhammer, J. Schmid, I. Mittermeier, F. Schreiber, L. Jiang, V. Pastuhovic, C. Herr, S. Heinze, International Journal of Hygiene and Environmental Health Extreme weather events in europe and their health consequences – A systematic review, Int. J. Hyg. Environ. Health. 233 (2021), https://doi.org/10.1016/j.ijheh.2021.113688.

[5] D. Leonhardt, Extreme Summer, New Yorks Times. (2021). https://www.nytimes.com/2021/07/20/briefing/heatwave-american-west-climate-change.html (accessed July 20, 2021).

[6] R. Kotharkar, A. Ramesh, A. Bagade, Urban Heat Island studies in South Asia: A critical review, Urban Clim. 24 (2018) 1011–1026, https://doi.org/10.1016/j.uclim.2017.12.006.

[7] R. Giridharan, R. Emmanuel, The impact of urban compactness, comfort strategies and energy consumption on tropical urban heat island intensity: A review, Sustain. Cities Soc. 40 (2018) 677–687, https://doi.org/10.1016/j.scs.2018.01.024.

[8] G. Xu, H. Xia, P. Chen, W. She, H. Zhang, J. Ma, Q. Ruan, W. Zhang, Z. Sun, Thermochromic Hydrogels with Dynamic Solar Modulation and Regulatable Critical Response Temperature for Energy-Saving Smart Windows, Adv. Funct. Mater. 32 (2022) 2109597, https://doi.org/10.1002/adfm.202109597.

[9] X. Pan, L. Shen, A.P.H.J. Schenning, C.W.M. Bastiaansen, Transparent, High-Thermal-Conductivity Ultradrawn Polyethylene/Graphene Nanocomposite Films, Adv. Mater. 31 (2019) 1–7, https://doi.org/10.1002/adma.201904348.

[10] X. Huang, X. Chen, A. Li, D. Atinafu, H. Gao, W. Dong, G. Wang, Shape-stabilized phase change materials based on porous supports for thermal energy storage applications, Chem. Eng. J. 356 (2019) 641–661, https://doi.org/10.1016/j.cej.2018.09.013.

[11] X. Li, J. Peoples, P. Yao, X. Ruan, Ultrawhite BaSO4Paints and Films for Remarkable Daytime Subambient Radiative Cooling, ACS Appl. Mater. Interfaces. 13 (2021) 21733–21739, https://doi.org/10.1021/acsami.1c02368.

[12] X. Sun, Y. Sun, Z. Zhou, M.A. Alam, P. Bermel, Radiative sky cooling: Fundamental physics, materials, structures, and applications, Nanophotonics. 6 (2017) 997–1015, https://doi.org/10.1515/nanoph-2017-0020.

[13] B. Zhao, M. Hu, X. Ao, N. Chen, G. Pei, Radiative cooling: A review of fundamentals, materials, applications, and prospects, Appl. Energy. 236 (2019) 489–513, https://doi.org/10.1016/j.apenergy.2018.12.018.

[14] J. Mandal, Y. Yang, N. Yu, A.P. Raman, Paints as a Scalable and Effective Radiative Cooling Technology for Buildings, Joule. 4 (2020) 1350–1356, https://doi.org/10.1016/j.joule.2020.04.010.

[15] X. Yu, J. Chan, C. Chen, Review of radiative cooling materials: Performance evaluation and design approaches, Nano Energy. 88 (2021), https://doi.org/10.1016/j.nanoen.2021.106259.

[16] X. Xue, M. Qiu, Y. Li, Q.M. Zhang, S. Li, Z. Yang, C. Feng, W. Zhang, J. Dai, D. Lei, W. Jin, L. Xu, T. Zhang, J. Qin, H. Wang, S. Fan, Creating an Eco-Friendly Building Coating with Smart Subambient Radiative Cooling, Adv. Mater. 32 (2020) 1906751, https://doi.org/10.1002/adma.201906751.

[17] T. Li, Y. Zhai, S. He, W. Gan, Z. Wei, M. Heidarinejad, D. Dalgo, R. Mi, X. Zhao, J. Song, J. Dai, C. Chen, A. Aili, A. Vellore, A. Martini, R. Yang, J. Srebric, X. Yin, L. Hu, A radiative cooling structural material, Science (80-.). 364 (2019) 760–763, https://doi.org/10.1126/science.aau9101.

[18] D. Lee, M. Go, S. Son, M. Kim, T. Badloe, H. Lee, J.K. Kim, J. Rho, Sub-ambient daytime radiative cooling by silica-coated porous anodic aluminum oxide, Nano Energy. 79 (2021), https://doi.org/10.1016/j.nanoen.2020.105426.

[19] Y. Wu, P. Krishnan, M.H. Zhang, L.E. Yu, Using photocatalytic coating to maintain solar reflectance and lower cooling energy consumption of buildings, Energy Build. 164 (2018) 176–186, https://doi.org/10.1016/j.enbuild.2018.01.011.

[20] Z. Sun, Q. Ye, C. Chi, J. Wu, Low band gap polycyclic hydrocarbons: From closed-shell near infrared dyes and semiconductors to open-shell radicals, 2012. 10.1039/c2cs35211g.

[21] N.N. Shi, C.C. Tsai, F. Camino, G.D. Bernard, N. Yu, R. Wehner, Keeping cool: Enhanced optical reflection and radiative heat dissipation in Saharan silver ants, Science (80-.). 349 (2015) 298–301, https://doi.org/10.1126/science.aab3564.

[22] X. Xue, Z. Yang, Y. Li, P. Sun, Y. Feng, Z. He, T. Qu, J.G. Dai, T. Zhang, J. Qin, L. Xu, W. Zhang, Superhydrophobic self-cleaning solar reflective orange-gray paint coating, Sol. Energy Mater. Sol. Cells. 174 (2018) 292–299, https://doi.org/10.1016/j.solmat.2017.09.014.

[23] B. Yuan, C. Straub, S. Segers, Q.L. Yu, H.J.H. Brouwers, Sodium carbonate activated slag as cement replacement in autoclaved aerated concrete, Ceram. Int. 43 (2017) 6039–6047, https://doi.org/10.1016/j.ceramint.2017.01.144.

[24] W. Kurdowski (Ed.), Cement and Concrete Chemistry, Springer Netherlands, Dordrecht, 2014.

[25] Y. Qin, Y. Zhao, X. Chen, L. Wang, F. Li, T. Bao, Moist curing increases the solar reflectance of concrete, Constr. Build. Mater. 215 (2019) 114–118, https://doi.org/10.1016/j.conbuildmat.2019.04.164.

[26] A.M. Kaja, H.J.H. Brouwers, Q.L. Yu, NOx degradation by photocatalytic mortars: The underlying role of the CH and C-S-H carbonation, Cem. Concr. Res. 125 (2019), https://doi.org/10.1016/j.cemconres.2019.105805.

[27] D. Liu, A. Kaja, Y. Chen, H.J.H. Brouwers, Q. Yu, Self-cleaning performance of photocatalytic cement mortar: Synergistic effects of hydration and carbonation, Cem. Concr. Res. 162 (2022), https://doi.org/10.1016/j.cemconres.2022.107009.

[28] C. Naber, S. Stegmeyer, D. Jansen, F. Goetz-Neunhoeffer, J. Neubauer, The PONKCS method applied for time resolved XRD quantification of supplementary cementitious material reactivity in hydrating mixtures with ordinary Portland cement, Constr. Build. Mater. 214 (2019) 449–457, https://doi.org/10.1016/j.conbuildmat.2019.04.157.

[29] J. Lv, H. Xu, M. Zhu, Y. Dai, H. Liu, Z. Li, The performance and model of porous materials in the indirect evaporative cooling system: A review, J. Build. Eng. 41 (2021), https://doi.org/10.1016/j.jobe.2021.102741.

[30] S.I. Igarashi, A. Watanabe, M. Kawamura, Evaluation of capillary pore size characteristics in high-strength concrete at early ages, Cem. Concr. Res. 35 (2005) 513–519, https://doi.org/10.1016/j.cemconres.2004.06.036.

[31] M. Auroy, S. Poyet, P. Le Bescop, J.M. Torrenti, T. Charpentier, M. Moskura, X. Bourbon, Comparison between natural and accelerated carbonation (3% CO2): Impact on mineralogy, microstructure, water retention and cracking, Cem. Concr. Res. 109 (2018) 64–80, https://doi.org/10.1016/j.cemconres.2018.04.012.

[32] M. Fernández Bertos, S.J.R. Simons, C.D. Hills, P.J. Carey, A review of accelerated carbonation technology in the treatment of cement-based materials and sequestration of CO2, J. Hazard. Mater. 112 (2004) 193–205, https://doi.org/10.1016/j.jhazmat.2004.04.019.

[33] G173–03: Standard Tables For Reference Solar Spectral Irradiances: Direct Normal And Hemispherical On 37° Tilted Surface, ASTM International, the US, 2003.

[34] L. Alados-Arboledas, Estimation of hourly values of downward atmospheric radiation under cloudless skies during day- and night-time conditions, Theor. Appl. Climatol. 48 (1993) 127–131, https://doi.org/10.1007/BF00864919.

[35] I. Galan, F.P. Glasser, D. Baza, C. Andrade, Assessment of the protective effect of carbonation on portlandite crystals, Cem. Concr. Res. 74 (2015) 68–77, https://doi.org/10.1016/j.cemconres.2015.04.001.

[36] G. Lu, W. She, X. Tong, W. Zuo, Y. Zhang, Radiative cooling potential of cementitious composites: Physical and chemical origins, Cem. Concr. Compos. 119 (2021), https://doi.org/10.1016/j.cemconcomp.2021.104004.

[37] E. Güler, G. Uğur, Ş. Uğur, M. Güler, A theoretical study for the band gap energies of the most common silica polymorphs, Chinese, J. Phys. 65 (2020) 472–480.

[38] F.M. Hossain, G.E. Murch, I.V. Belova, B.D. Turner, Electronic, optical and bonding properties of CaCO3 calcite, Solid State Commun. 149 (2009) 1201–1203, https://doi.org/10.1016/j.ssc.2009.04.026.

[39] R. Levinson, H. Akbari, Effects of composition and exposure on the solar reflectance of portland cement concrete, Cem. Concr. Res. 32 (2002) 1679–1698, https://doi.org/10.1016/S0008-8846(02)00835-9.

[40] K.U. Ambikakumari Sanalkumar, E.H. Yang, Self-cleaning performance of nano-TiO2 modified metakaolin-based geopolymers, Cem. Concr. Compos. 115 (2021), https://doi.org/10.1016/j.cemconcomp.2020.103847.

[41] Y. Wu, P. Krishnan, L.E. Yu, M.H. Zhang, Using lightweight cement composite and photocatalytic coating to reduce cooling energy consumption of buildings, Constr. Build. Mater. 145 (2017) 555–564, https://doi.org/10.1016/j.conbuildmat.2017.04.059.

[42] E. Enríquez, M. Torres-Carrasco, M.J. Cabrera, D. Muñoz, J.F. Fernández, Towards more sustainable building based on modified Portland cements through partial substitution by engineered feldspars, Constr. Build. Mater. 269 (2021), https://doi.org/10.1016/j.conbuildmat.2020.121334.

[43] H.Y. Ma, I.S. Lee, Characterization of vaterite in low quality freshwater-cultured pearls, Mater. Sci. Eng. C. 26 (2006) 721–723, https://doi.org/10.1016/j.msec.2005.09.109.

[44] M.I. Daskalakis, F. Rigas, A. Bakolas, A. Magoulas, G. Kotoulas, I. Katsikis, A.P. Karageorgis, A. Mavridou, Vaterite bio-precipitation induced by Bacillus pumilus isolated from a solutional cave in Paiania, Athens, Greece, Int. Biodeterior. Biodegrad. 99 (2015) 73–84, https://doi.org/10.1016/j.ibiod.2014.12.005.

[45] T. Bao, Z.(. Liu, X. Zhang, Y. He, A drainable water-retaining paver block for runoff reduction and evaporation cooling, J. Clean. Prod. 228 (2019) 418–424.

[46] M. Saffari, C. Piselli, A. de Gracia, A.L. Pisello, F. Cotana, L.F. Cabeza, Thermal stress reduction in cool roof membranes using phase change materials (PCM), Energy Build. 158 (2018) 1097–1105, https://doi.org/10.1016/j.enbuild.2017.10.068.

[47] X. Xue, J. Yang, W. Zhang, L. Jiang, J. Qu, L. Xu, H. Zhang, J. Song, R. Zhang, Y. Li, J. Qin, Z. Zhang, The study of an energy efficient cool white roof coating based on styrene acrylate copolymer and cement for waterproofing purpose - Part I: Optical properties, estimated cooling effect and relevant properties after dirt and accelerated exposures, Constr. Build. Mater. 98 (2015) 176–184, https://doi.org/10.1016/j.conbuildmat.2015.08.045.

[48] Y. Du, P. Liu, X. Quan, C. Ma, Characterization and cooling effect of a novel cement-based composite phase change material, Sol. Energy. 208 (2020) 573–582, https://doi.org/10.1016/j.solener.2020.07.083.

[49] G. Chen, Y. Wang, J. Qiu, J. Cao, Y. Zou, S. Wang, D. Jia, Robust Inorganic Daytime Radiative Cooling Coating Based on a Phosphate Geopolymer, (2020). 10.1021/acsami.0c15799.